Nuclear level density and γ decay strength of ^{93}Sr

A. Sweet,[1,*] D. L. Bleuel,[1] N. D. Scielzo,[1] L. A. Bernstein,[2,3] A. C. Dombos,[4,5,6] B. L. Goldblum,[2,3] C. M. Harris,[4,5,6] T. A. Laplace,[2] A. C Larsen,[7] R. Lewis,[4] S. N. Liddick,[4,8] S. M. Lyons,[4] F. Naqvi,[4] A. Palmisano-Kyle,[4,6,5] A. L. Richard,[1,†] M. K. Smith,[4] A. Spyrou,[4,5,6] J. Vujic,[2] and M. Wiedeking[9,10]

[1]*Lawrence Livermore National Laboratory (LLNL), Livermore, California 94551, USA*
[2]*Department of Nuclear Engineering, University of California, Berkeley (UCB), California 94720, USA*
[3]*Lawrence Berkeley National Laboratory (LBNL), Berkeley, California 94720, USA*
[4]*Facility for Rare Isotope Beams (FRIB)/National Superconducting Cyclotron Laboratory (NSCL), Michigan State University (MSU), East Lansing, Michigan 48824, USA*
[5]*Department of Physics and Astronomy, Michigan State University (MSU), East Lansing, Michigan 48824, USA*
[6]*Joint Institute for Nuclear Astrophysics (JINA), Michigan State University (MSU), East Lansing, Michigan 48824, USA*
[7]*Department of Physics, University of Oslo (UiO), N-0316 Oslo, Norway*
[8]*Department of Chemistry, Michigan State University MSU(), East Lansing, Michigan 48824, USA*
[9]*Department of Subatomic Physics, iThemba LABS, Somerset West 7129, South Africa*
[10]*School of Physics, University of the Witwatersrand, Johannesburg 2050, South Africa*

(Dated: January 6, 2024)

This work presents the first experimentally-determined nuclear level density and γ-ray strength function of the short-lived fission product ^{93}Sr, accomplished using the β-Oslo Method. Direct measurement of the ^{92}Sr(n,γ)^{93}Sr cross section is not currently possible, as the half-life of 2.66 hours is too short; instead, ^{93}Sr was formed through β decay of ^{93}Rb to excitation energies around the neutron separation energy. The γ-ray spectra were measured using a total absorption spectrometer at the National Superconducting Cyclotron Laboratory (NSCL) at Michigan State University (MSU). The statistical properties of the ^{93}Sr nucleus were experimentally determined, including the γ-ray strength function and nuclear level density. At low energies, the γ-ray strength function exhibits a constant γ-decay strength, rather than a slightly increasing strength with decreasing γ-ray energy as had been previously observed for several nuclei in this mid-mass region. These statistical properties were then implemented in the reaction code TALYS1.95 to calculate the ^{92}Sr(n,γ)^{93}Sr cross section.

I. INTRODUCTION

Understanding the production and destruction pathways of exotic nuclei has far-reaching impacts on nuclear physics applications, from cosmogenic nucleosynthesis to supporting the science-based U.S. Stockpile Stewardship mission [1]. Direct measurement of the reaction cross sections of interest is typically not possible as these isotopes are available only in limited quantities and are often too short-lived to be made into a target. Alternatively, the reaction cross sections can be inferred from statistical nuclear properties, which can be determined with indirect methods such as the surrogate method [2, 3] or the Oslo and β-Oslo Method [4–6].

Statistical nuclear properties for exotic nuclei, such as the Nuclear Level Density (NLD) and γ-ray Strength Function (γSF), calculated through theoretical predictions utilizing extrapolations from experimental data for stable nuclei are charactered by large systematic uncertainties [7]. In contrast, by employing the β-Oslo Method to extract the NLD and γSF from the experimentally measured γ-ray emission data, these statistical nuclear properties can be constrained as much as by an order of magnitude. The Oslo Method and the β-Oslo Method assume the γ decay of excited nuclear states formed through a charged-particle reaction or β decay, respectively, is independent of how the excited state was formed, on average [4, 8].

Nuclei with a β-decay Q_β value approximately equal to the neutron-separation energy of the daughter nucleus generally make the quasi-continuum experimentally accessible. By using a high-efficiency total absorption spectrometer, the complete γ-ray cascade can be detected, allowing for the identification of the initial excitation energy populated by each β decay. From the measured γ-ray spectra following β decay, the NLD and γSF can be experimentally extracted using the β-Oslo Method; however, normalizing these nuclear statistical properties to auxiliary nuclear-resonance data includes a known systematic uncertainty that has been investigated and addressed by Ref. [9]. Previously, the Oslo Method has been successfully applied to a wide mass range from ^{44}Sc to ^{243}Pu [10], while the β-Oslo Method, which was first implemented to experimentally-determine the ^{75}Ge(n,γ)^{76}Ge [6] cross section, was benchmarked by comparing results of this indirect technique to the directly measured ^{50}Ti(n,γ)^{51}Ti reaction [11].

As the NLD and γSF are key parameters in the Hauser-Feshbach formalism, these experimentally-determined nuclear inputs directly impact the calculated neutron-capture cross section [12]. The cross sections for neutron-induced reactions, such as neutron-capture reactions, are

* Formerly: UCB
† Formerly: FRIB/NSCL

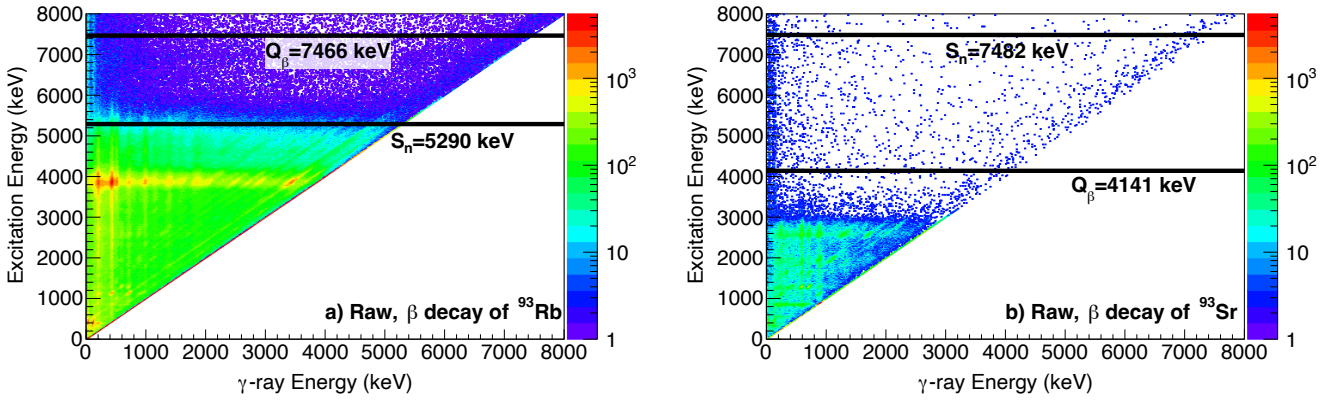

FIG. 1. Raw β-Oslo matrices comprising of the initial experimentally-measured γ-ray energies and excitation energies from β-γ coincidences detected using SuNTAN highlight the difference in Q_β-value between the decay of ^{93}Rb and ^{93}Sr. The Q_β values for ^{93}Rb and ^{93}Sr as well as the S_n values for ^{93}Sr and ^{93}Y are indicated by black horizontal lines, respectively. (a) The raw matrix of ^{93}Rb decay was obtained from 60 s implantation periods of the thermal ^{93}Rb beam and the subsequent subtraction of (b) the raw ^{93}Sr decay matrix. The raw ^{93}Sr decay matrix was obtained by measuring the decay following an implantation period of 30 min. The decay of ^{93}Rb populated higher excitation energies compared to the decay of ^{93}Sr.

essential nuclear data that underpin nuclear-security and nuclear energy applications [1]. In addition, the formation of heavy elements with A >60 in the cosmos was driven by neutron-capture reactions, and understanding these processes requires accurate and reliable nuclear masses, β-decay properties, as well as neutron capture and fission rates [13, 14]. When neutron capture occurs more slowly than β-decay rates, nuclei that lie along the valley of stability are produced, which is described as the slow-neutron capture process (*s process*) [15]. In contrast, when neutron capture occurs more rapidly than β-decay rates, heavy nuclei are produced by the rapid-neutron capture process (*r process*) [15]. Of these processes, the r process occurring in a high neutron flux environment leads to the formation of neutron-rich isotopes far from stability [13]. Astrophysical observations show that the abundances of heavy elements in the solar system match those observed in many metal-poor halo stars, with the exception of certain lighter heavy elements, such as Rb, Sr, Y, and Zr [13, 16]. One possible explanation for this observation might be an *intermediate (i) process* [16]. From an i-process sensitivity study, the ^{92}Sr(n,γ)^{93}Sr reaction was identified as an important production pathway contributing to the Zr abundance [16].

Moreover, the distribution of fission products observed following a nuclear chain reaction provides key diagnostics that support the U.S. science-based Stockpile Stewardship mission [1]. However, the yields of these long-lived fission products may be influenced by the burnup of the short-lived fission products made directly from fission in a complicated network of production and destruction reactions that can occur in a high-neutron-flux environment. For the short-lived fission products, which are many neutrons from stability, the reaction rates are uncertain and rely entirely upon theoretical predictions. This work constrains the ^{92}Sr(n,γ)^{93}Sr cross section which will assist in improving our understanding of the reaction network that influences the abundance of ^{95}Zr, used as a diagnostic tool to determine the number of fissions [1].

II. EXPERIMENTAL DETAILS

A radioactive stopped-beam experiment was performed at the National Superconducting Cyclotron Laboratory (NSCL) to constrain the ^{92}Sr(n,γ)^{93}Sr cross section. The Coupled Cyclotron Facility at the NSCL produced a primary beam of ^{96}Zr at 120 MeV per nucleon, which impinged on a 394 mg/cm^2 ^{9}Be target producing a secondary beam with the projectile fragmentation technique [17]. The secondary beam was purified using the A1900 fragment separator to produce a high-purity beam of radioactive ^{93}Rb [18]. The ^{93}Rb beam was sent through the Gas Stopping Facility, where it was thermalized, extracted at 30 keV, and delivered to the Summing NaI(Tl) (SuN) detector in the stopped beam area [19, 20].

A new beamline in the stopped beam area delivered the ^{93}Rb beam to an experimental detector system, which consisted of a total absorption spectrometer known as the SuN detector, a plastic scintillator barrel (fiber detector), and a tape transport system for removing daughter activity (SuNTAN) [21]. The SuN detector is a large volume cylindrical detector, 16 inches in height and diameter, composed of eight optically-isolated segments each with three photomultiplier tubes (PMTs). A 1.8 in borehole along its axis allows for the 3-mm-thin fiber detector to

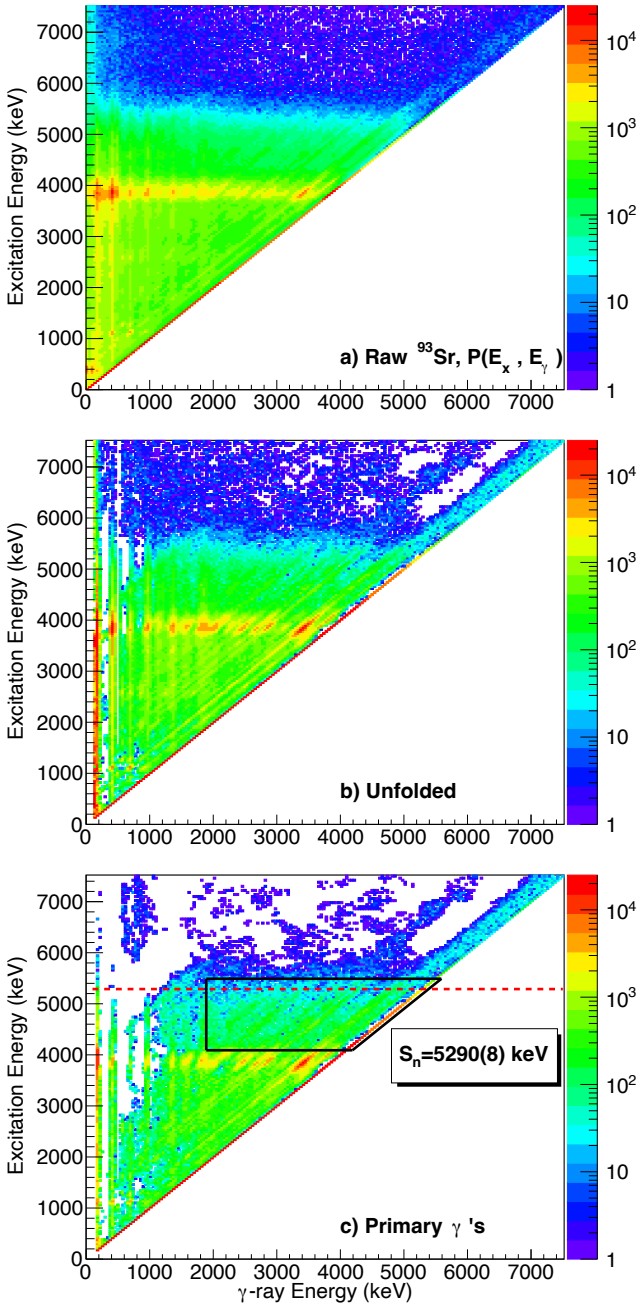

FIG. 2. (a) Raw, (b) unfolded, and (c) primary ^{93}Sr(E_x, E_γ) matrices from the measured β-γ coincidence of ^{93}Rb decay. The bin width of the horizontal and vertical axes is 40 keV. The trapezoid shown in the primary matrix marks the γ-ray and excitation energy thresholds while the red dashed line signifies the neutron separation energy, S_n.

be placed in the center inside the beam line, which connects to two PMTs outside SuN through fiberoptic cables. The ^{93}Rb ions were implanted in the tape at the center of this detector system.

The fiber detector was used to identify the emitted β particles. The $\beta - \gamma$ coincidences and the technique of total absorption spectroscopy (TAS) were utilized to determine the β-populated excited states in the decay daughter and exclude background γ rays. SuN was used to efficiently detect individual γ rays, as well as determine from the sum of these γ-ray energies E_γ, the excitation energy E_x of the daughter nucleus following β decay.

Following the decay of ^{93}Rb (Q_β = 7.466(9) MeV, $t_{1/2}$ = 5.84(2) s), the daughter nucleus ^{93}Sr also β decays (Q_β = 4.141(12) MeV, $t_{1/2}$ = 7.43(3) min) to the longer lived daughter ^{93}Y (Q_β = 2.895(10) MeV, $t_{1/2}$ = 10.18(8) h). With the SuNTAN system, an implantation period of 60 s followed by the removal and replacement of tape within the system was implemented to minimize the counts from the ^{93}Sr β decay to less than approximately 4% of observed β decays according to the Bateman equations [22, 23]. This competing radiation was characterized using longer SuNTAN tape cycles, where the ^{93}Rb nuclei were implanted for 30 min followed by a measuring period of 20 mins with the beam off. Within one minute of the beam off period, the β decay of ^{93}Rb was reduced to near zero and the counting period that followed measured the ^{93}Sr β decay.

The $\beta - \gamma$ coincidence matrix for the ^{93}Sr β decay, referred to as $D(E_x, E_\gamma)$, is subtracted from the sum of 60 s accumulation periods represented by the $\beta - \gamma$ coincidence matrix $M(E_x, E_\gamma)$ of measured ^{93}Rb β decays, through applying a scaling factor $N = 4.0\%$:

$$M(E_x, E_\gamma) - \frac{N \int\int M(E_x, E_\gamma) dE_x dE_\gamma}{\int\int D(E_x, E_\gamma) dE_x dE_\gamma} D(E_x, E_\gamma) = P(E_x, E_\gamma) \quad (1)$$

to obtain the subtracted $\beta - \gamma$ coincidence matrix $P(E_x, E_\gamma)$. The β decay of ^{93}Sr yields lower-energy γ rays due to the lower Q_{β^-} value and the large β-decay transition strengths to states below 3 MeV [24]. Consequently, the competing radiation from the β decay of ^{93}Sr predominately affects the γ-ray energy distribution below 3 MeV.

The resulting $P(E_x, E_\gamma)$ of ^{93}Rb β decay is shown in Fig. 1a and is compared to the competing radiation matrix $D(E_x, E_\gamma)$ in Fig. 1b. These plots illustrate the significant difference in neutron separation energy between ^{93}Sr and ^{93}Y. In addition, there is a decrease in data collect from 3 MeV to 4 MeV for ^{93}Sr β decay shown in Fig. 1b due to low β-decay feeding. The ^{93}Rb matrix extends beyond the neutron separation energy $S_n(^{93}\text{Sr}) = 5.290(8)$ MeV due to the high Q_{β^-} [24]. Subsequently, populating states in the continuum may lead to β-delayed neutron emission. Despite this, the β-delayed neutron branch is low, $I_{\beta n}$ = 1.39%, and the delayed neutron populates most significantly the ground state of ^{92}Sr with a 87.5(19)% intensity and the first excited state at 814.98 keV with 12.5(19)% [25]. Competing radiation from β-delayed neutron emission along with the β decay of ^{93}Sr influenced which region of excitation energy and γ-ray energy was selected for analysis using the β-Oslo Method by directing the choice of upper and lower bound energy limits. Outside these limits, data

would not be representative of the γ decay following β decay of ^{93}Rb.

The β-Oslo Method is applied to a select region of excitation energy and γ-ray energy referred to as the region of interest (ROI). In this case, the ROI is bound by the E_γ >1.89 MeV and 4.09 < E_x < 5.49 MeV, which is representative of statistical γ decay from the quasi-continuum. Moreover, the ROI excludes measured γ rays and excitation energies potentially from the β-delayed neutron daughter ^{92}Sr. The first excited state of ^{92}Sr is relatively high, thus the upper E_x threshold of the ROI may be as high as 6.10 MeV and still exclude contamination from the γ decay of ^{92}Sr. Ultimately, the upper E_x threshold was chosen to be 5.49 MeV due to poor statistics at higher E_x in the $P(E_x, E_\gamma)$ matrix. By subtracting the competing radiation from the raw experimental matrix, $M(E_x, E_\gamma)$, the resulting $\beta - \gamma$ coincidence matrix, $P(E_x, E_\gamma)$, contains approximately 0.2% fewer counts within the ROI, or 436,000 counts. Finally, the $P(E_x, E_\gamma)$ matrix can be analyzed using the β-Oslo Method.

III. ANALYSIS METHOD: β-OSLO METHOD

The ^{93}Rb β-decay matrix shown in Fig. 2a was analyzed using a four-step technique known as the β-Oslo Method. The first two steps we use to analyze this experimental matrix are (*i*) unfolding the raw γ-ray spectra using the known response function of the SuN detector [19, 21] and (*ii*) extracting the primary γ-ray matrix using an iterative subtraction technique developed by Ref. [4]. Once the primary γ-ray matrix is obtained, the last two steps are to (*iii*) extract the NLD and the γSF from the ROI represented by the trapezoidal region in Fig. 2c and (*iv*) normalize them using additional external nuclear data. The β-Oslo Method relies on the assumption that the distribution of γ rays for an excitation-energy region, on average, is independent of the population mechanism [4]. In addition, Ref. [9] highlights possible systematic errors in each of the four steps of the standard Oslo Method [5], which are similarly applicable to the β-Oslo Method with the exceptions of using the TAS technique that includes the complication of incomplete summing, additional background from β-decay electrons, and normalization of the NLD and γSF.

The β-Oslo Method begins with the unfolding of γ-ray spectra using the folding iterative method described in Ref. [26], followed by a Compton subtraction method utilizing the detector response function. The response function for the SuNTAN-fiber detector system, representing the response of individual segments to γ rays detected in coincidence with β particles, was generated using the GEANT4 simulation toolkit [19, 27] and calibrated with a set of standard radioactive sources. The unfolded matrix shown in Fig. 2b represents the distribution of primary γ rays as well as the γ rays that originate from later steps in the decay cascade for each excitation energy bin.

From the unfolded matrix, higher generation γ rays in each excitation-energy bin were removed using an iterative subtraction method. The method begins with the unfolded γ-ray spectrum of bin i, f_i, which is projected out on the γ-ray energy axis from the unfolded matrix, and a weighted sum of the spectra for all underlying energy bins $j = 0, 1, ..., i-1$. The weighted sum of all underlying spectra, g_i, contains the same γ transitions as spectrum f_i except for those from bin i to bins $j = 0, 1, ..., i-1$. For a given excitation energy bin, the spectrum of primary γ rays is obtained by subtracting g_i from the unfold spectrum, where the weighting coefficient is the branching ratio of each primary γ ray as described in Ref. [5]. In Fig. 2c, the primary matrix displays a strong diagonal, which represents the energy deposited by emission of a single γ ray with energy equal to the excitation energy, $E_x = E_\gamma$, as well as background events from the electrons emitted in the β decay. This strong diagonal is also visible in the unfolded matrix. In Sec. IV B, this work later demonstrates that analysis of ROI sub-regions that exclude several diagonals results in a γSF that reasonably agrees with the extracted γSF from the total ROI.

The primary γ-ray matrix shown in Fig. 2c represents the probability $P(E_x, E_\gamma)$ of emitting γ rays of energy E_γ from excited states at energies around E_x. $P(E_x, E_\gamma)$ is proportional to two independent functions: the NLD at the final excitation energy, $\rho(E_x - E_\gamma = E_f)$, and the transmission coefficient, $\mathcal{T}(E_\gamma)$. From the work of A. Schiller *et al.* in Ref. [5], an expression was developed for this relationship:

$$P(E_x, E_\gamma) \propto \rho(E_f)\mathcal{T}(E_\gamma). \tag{2}$$

Additionally, the radiative strength is dominated by dipole transitions, thus the γSF, $f(E_\gamma)$, is obtained from a direct proportionality to $\mathcal{T}(E_\gamma)$:

$$f(E_\gamma) = \frac{\mathcal{T}(E_\gamma)}{2\pi E_\gamma^3}. \tag{3}$$

From the ROI, these functions are extracted simultaneously using the proportionality as presented in Eq. 2 and a least χ^2 method [5]. This method compares the experimental primary matrix $P(E_x, E_\gamma)$ to a theoretical primary generation matrix $P_{th}(E_x, E_\gamma)$ that can be can be approximated as

$$P_{th}(E_x, E_\gamma) = \frac{\rho(E_x)\mathcal{T}(E_\gamma)}{\sum_{E'_\gamma = E_\gamma^{min}}^{E_x} \rho(E_x - E'_\gamma)\mathcal{T}(E'_\gamma)}. \tag{4}$$

This method of extracting the functional forms of $\rho(E_x - E_\gamma)$ and $\mathcal{T}(E_\gamma)$ through an iterative procedure is described in Ref. [5]. Possible systematic errors of the method have been discussed previously in Ref. [9]. In particular, very low statistics at high E_x resulted in an unreliable χ^2 minimization, and thus, low-statistics regions should to be excluded.

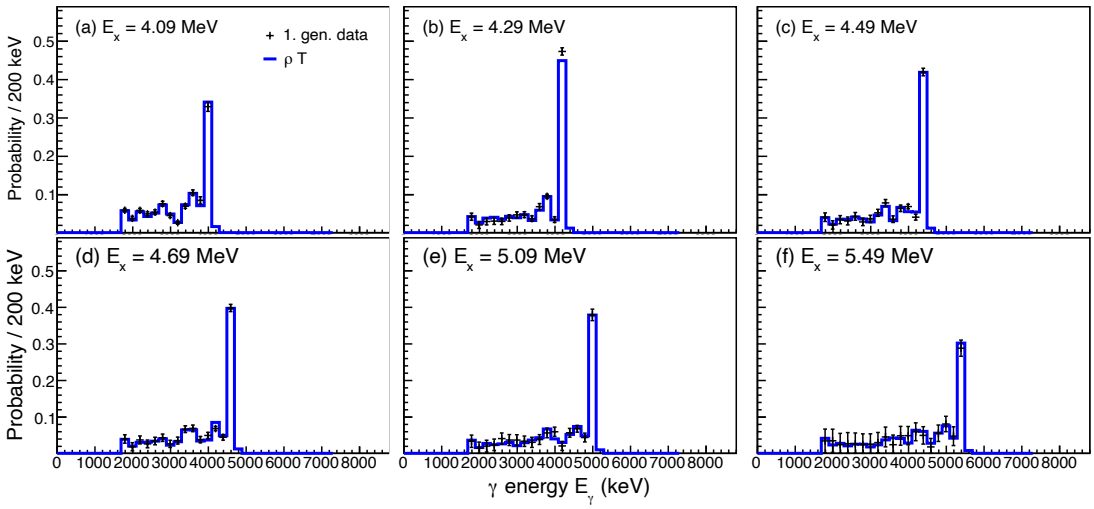

FIG. 3. Comparison between experimental (black crosses) and calculated (blue line) primary γ spectra for individual excitation energy bins within the region of interest E_x=4.09-5.49 MeV.

The method of extracting the NLD and γSF relies on the assumption that the generalized Brink-Axel hypothesis [28, 29] is valid, implying the γSF is dependent purely on the γ-ray energy, E_γ. For heavy nuclei, the generalized Brink-Axel hypothesis in the case of ^{238}Np was experimentally verified to be valid in Ref. [30]. In addition, for light nuclei, the works of M. Guttormsen *et al.* in Ref. [31] and L. Crespo Campo *et al.* in Ref. [32] tested the validity of the generalized Brink-Axel hypothesis for ^{46}Ti and ^{64,65}Ni, demonstrating that the γSFs are independent of the initial excitation energy even in cases of a low level density at the neutron separation energy. From the findings of these works, the assumption can then be made that the generalized Brink-Axel hypothesis is valid for ^{93}Sr, which has a similar level density to ^{64,65}Ni.

Solutions to $P(E_x, E_\gamma)$ must be normalized to additional external nuclear data because the initial extraction approach does not sufficiently constrain the NLD and γSF. As was shown in Ref. [5], an infinite number of functions can be construction from the extracted $\rho(E_x - E_\gamma)$ and $\mathcal{T}(E_\gamma)$ using three parameters: A, B, and α, are expressed as

$$\tilde{\rho}(E_f) = A\rho(E_f)e^{\alpha E_f}, \quad (5)$$

$$\tilde{\mathcal{T}}(E_\gamma) = B\mathcal{T}(E_\gamma)e^{\alpha E_\gamma}. \quad (6)$$

These normalization parameters: A, B, and α, are solved for using auxiliary nuclear data to determine the most physical solution.

The β decay of ^{93}Rb is a selective process that populates $3/2^-$, $5/2^-$, and $7/2^-$ levels in ^{93}Sr by Gamow-Teller β decay. Intense β-decay feeding to initial levels around $E_x = 3.88$ MeV was observed as indicated by the higher number of counts in this excitation region shown in Fig. 2c. This intensely populated region in our experimental matrix agrees with the reported β-decay intensities from Ref. [24]. Thus, these initial levels may introduce a non-statistical behavior to the NLD and γSF due to their similarity in spins. This potentially non-statistical decay from a grouping of similar states at approximately 3.88 MeV is excluded from the analysis by placing an excitation energy threshold at 4.09 MeV. The extraction method resulted in a χ^2 of 0.83 for the region of interest E_x=4.09-5.49 MeV, and the comparison between the experimental primary γ spectra $P(E_x, E_\gamma)$ and the calculated primary γ spectra $P_{th}(E_x, E_\gamma)$, which was obtained from the product of the extracted $\rho(E_x - E_\gamma)$ and $\mathcal{T}(E_\gamma)$, is shown in Fig. 3. For each individual excitation energy, agreement between the experimental and calculated spectra is visible with relatively few disagreements compared to previous β-Oslo Method experiments of the lighter nuclei ^{76}Ge and ^{51}Ti [6, 11], which suggests $\rho(E_f)$ and $\mathcal{T}(E_\gamma)$ were successfully extracted from a statistical region of the experimental primary γ spectra. The uncertainties in the data represent the statistical uncertainties plus an estimate of systematic errors due to the γ-ray spectrum unfolding and first-generation method.

IV. NORMALIZATION OF THE NLD AND γSF

Dipole transitions following the β decay of ^{93}Rb result in populating levels in ^{93}Sr with spins and parities of $1/2^\pm$, $3/2^\pm$, $5/2^\pm$, $7/2^\pm$, and $9/2^\pm$. The slope and magnitude of the NLD and γSF for ^{93}Sr are determined through normalization to auxiliary nuclear data as well as to an estimated reduction factor representing the subset of populated levels compared to all possible levels. The NLD normalization influences the shape of the γSF through parameter α; thus, the estimated level density

at the neutron separation energy, $\rho(S_n)$, for ^{93}Sr and the reduction factor are two significant sources of systematic uncertainty. Lastly, the magnitude of the γSF is obtained by normalizing the extracted function to the average, total radiative width of s-wave neutron resonances, $\langle\Gamma_\gamma\rangle$ using Eq. 7 of Ref. [33], which assumes that the main contributions to the γSF are the E1 and M1 transitions to accessible levels. In this section, several investigated normalization approaches are presented along with the resulting NLD and γSF obtained by this work.

A. Normalizing the NLD

In order to obtain the NLD normalization, we utilized the phenomenological and microscopic model techniques summarized here. The slope α and scaling factor A parameters are determined using discrete levels of ^{93}Sr reported by Ref. [24] and an estimated value for the level density at the neutron separation energy, $\rho(S_n)$. The level scheme of ^{93}Sr is considered complete up to 2.2 MeV, or 20 levels [36], beyond which the cumulative number of experimentally-identified levels ceases to increase exponentially as expected, but rather plateaus due to deficiencies in the experimental data. At low excitation energy, the experimental NLD for ^{93}Sr was fit to these discrete levels reported by Ref. [24]. At excitation energies near S_n, an estimated D_0 value was obtained using two approaches:

1. fitting global systematics developed by T. von Egidy and D. Bucurescu [34, 35, 38] to semi-experimental $\rho(S_n)$ values for neighboring nuclei ($norm1$), or

2. fitting a microscopic model calculation using the Hartree-Fock-Bogoliubov plus combinatorial (HFB + c) tabulated values [39] to discrete levels ($norm2$).

These approaches successfully constrained the NLD in a previous Oslo Method study of ^{89}Y [37] and in a benchmark experiment utilizing the β-Oslo Method to extract the NLD and γSF of ^{76}Ge [6]. Due to the proximity of ^{93}Sr to these nuclei, the work presented here utilized similar approaches as there are no experimental neutron resonance parameters for Sr isotopes far from stability.

As the experimentally extracted NLD for ^{93}Sr extends to only 3.6 MeV, the Constant Temperature (CT) formula was used to interpolate between the last data point and the estimated $\rho(S_n)$ value at high excitation energy. This approach was successful in describing other nuclei in the mass region such as ^{89}Y and ^{91,92}Zr [37, 40]. The estimated $\rho(S_n)$ value for ^{93}Sr was determined using a similar approach to Ref. [37], where predicted values from global systematics from Refs. [34, 35, 38] are fit to semi-experimental $\rho(S_n)$ of neighboring Rb, Sr, Y, and Zr nuclei. In this phenomenological-based $\rho(S_n)$ estimate, two formulations of the spin-cutoff parameters were considered. The first is the energy-dependent spin-cutoff parameter σ_{ED} as parameterized by Ref. [34]:

$$\sigma^2_{ED} = 0.391A^{0.675}(E_x - 0.5P_{a'})^{0.312}, \tag{7}$$

where, A is the mass number, E_x is the excitation energy, and $P_{a'}$ is the deuteron pairing energy. This work considered a second spin-cut off formulation, σ_{RMI}, the rigid-body moment of inertia approach:

$$\sigma^2_{RMI} = 0.0146A^{5/3}\frac{1+\sqrt{1+4a(E_x-E_1)}}{2a}. \tag{8}$$

According to Ref. [35], a is the level-density parameter and E_1 is the excitation-energy shift parameter. The calculated spin cut-off parameter along with experimental s-wave neutron level spacing D_0 values for the neighboring nuclei ^{86,88}Rb, ^{85,87,88,89}Sr, ^{90}Y, and $^{91-95,97}$Zr [36] were used to determine the semi-experimental $\rho(S_n)$ values by the expression [5]:

$$\rho(S_n) = \frac{2\sigma^2}{D_0}\times \frac{1}{(J_t+1)\exp[-(J_t+1)^2/2\sigma^2] + J_t\exp[-J_t^2/2\sigma^2]}, \tag{9}$$

where J_t is the spin of the target nucleus in a neutron-capture reaction. Fig. 4 of Ref. [37] illustrates the approach where global-systematic predictions for ^{89}Y are fit to semi-experimental $\rho(S_n)$ values to estimate $\rho(S_n)$ of ^{89}Y.

The comparison of global-systematic predictions for ^{93}Sr to semi-experimental $\rho(S_n)$ values of neighboring nuclei calculated using Eq. 9 is shown in Figs. 4a and 4b. The predictions were fit to semi-experimental $\rho(S_n)$ values of ^{86,88}Rb, ^{85,87,88,89}Sr, ^{90}Y, and $^{91-95,97}$Zr using a scaling factor as was done in Ref. [37]. In examining the systematics of this mass region, this work observed that using the spin cut-off parameter of the rigid-body moment of inertia model, σ_{RMI}, to estimate $\rho(S_n)$ resulted in a steeply sloped NLD for ^{93}Sr, and consequently, a steep γSF slope. A steeply sloped γSF such as this was compared to the Giant Dipole Resonance described by the resonance parameters of ^{88}Sr [36], and the mismatch observed guided this work to exclude the σ_{RMI} approach as it was not an adequate description at high excitation energy. In contrast, the energy-dependent spin-cutoff parameter σ_{ED} yielded lower estimated $\rho(S_n)$ of ^{93}Sr. The neighboring nuclei we included in our systematic study span a range of proton-neutron combinations; thus this work investigated two subsets of the neighboring nuclei: odd-A nuclei and Sr nuclei only. The scaling factor and corresponding upper and lower 1-σ uncertainty were $0.34^{+0.08}_{-0.07}$, $0.36^{+0.12}_{-0.11}$, and $0.33^{+0.08}_{-0.07}$, where the nuclei included were all neighboring nuclei, odd-A only, and Sr nuclei only, respectively. The estimated total level density of ^{93}Sr at $S_n = 5.290(8)$ MeV [24] using $\sigma_{ED} = 3.709$ was $\rho(S_n) = 1.35\times10^3$ MeV^{-1} for $D_0 = 21.15$ keV, and

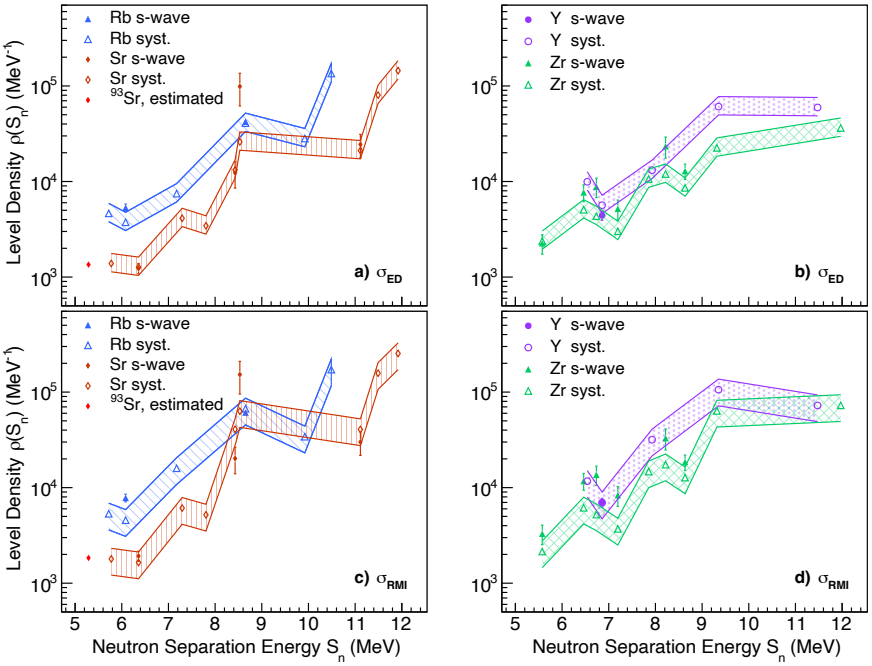

FIG. 4. Predicted level densities at S_n from global systematics of Refs. [34, 35] are compared to semi-experimental data for Rb, Sr, Y, and Zr nuclei. The semi-experimental data shown as filled points were calculated using experimental s-wave neutron level spacing D_0 values from Ref. [36] and (a & b) the energy-dependent spin-cutoff parameter σ_{ED} of Ref [34] or (c & d) the rigid-body moment of inertia σ_{RMI} of Ref. [35] in Eq. 9. The estimated $\rho(S_n)$ of ^{93}Sr is shown as a filled red diamond. The systematic study of this mass region was first published by Ref. [37] in Fig. 4.

the upper and lower uncertainties were used to set the normalization bounds: $\rho^{up}(S_n) = 1.96{\times}10^3$ MeV^{-1} for $D_0 = 14.54$ keV and $\rho^{low}(S_n) = 1.02{\times}10^3$ MeV^{-1} for $D_0 = 27.92$ keV. This methodology for estimating the $\rho(S_n)$ for the isotopes of interest from systematics of the mass region is similar to the approach used by Ref. [37].

In contrast to the phenomenological approach discussed, the HFB + c approach described by Ref. [39] was used to estimate $\rho(S_n)$ for ^{93}Sr from a fit of tabulated NLD values to discrete levels at low energy. The HFB + c tabulated NLD values can be shifted in energy by δ and in shape by c as so [41]:

$$\rho(E_x, J, \pi) = \rho_{HFB}(E_x - \delta, J, \pi)e^{c\sqrt{E_x - \delta}}. \quad (10)$$

The tabulated NLD was shifted by δ to determine the best agreement with the 20 known discrete levels of ^{93}Sr using a χ^2 approach, which resulted in a value of δ=0.162, yielding $\rho(S_n) = 4.866{\times}10^3$ MeV^{-1} with $D_0 = 6.02$ keV and a spin cut-off $\sigma_{HFB+c} = 3.76$. The $\rho_{HFB+c}(S_n)$ value results in a steep slope for the NLD, and thus, as was the case in using σ_{RMI}, a steep γSF. Ultimately, the HFB + c approach, *i.e.*, *norm*2, was not used in the resulting experimentally-determined ^{92}Sr(n,γ)^{93}Sr cross section.

The slope parameter α was initially obtained from the normalization of the NLD. Due to the spin-selectivity of β decay, the resulting observed NLD represents only part of the total NLD, and thus is described by a different slope. Consequently, the slope of the extracted γSF is determined from a reduced NLD representative of the spins populated by the β-delayed primary γ rays, which resulted in an expanded spin window by $\pm\hbar$. In this work, the reduction factor for the NLD at S_n was obtained from the ratio of populated levels to the intrinsic number of levels. The spin distribution as a function of excitation energy can be expressed as [42]

$$g(E_x, J) = \frac{2J+1}{2\sigma^2} e^{\left[\frac{-(J+1/2)^2}{2\sigma^2}\right]}. \quad (11)$$

The ratio of populated levels to the intrinsic level distribution determined through the HFB+c approach was 66%, which served as a reduction factor of the *norm*2 NLD normalization point, $\rho(S_n)$. In comparison, the phenomenological approach yielded a similar reduction factor of 67% for *norm*1. This reduced level density at S_n and a reduced number of discrete levels at low energies representative of the populated levels due the β-delayed primary γ rays is then used to determine the slope of γSF. In Refs. [6, 11], this approach was applied successfully to ^{76}Ge and ^{51}Ti.

As both approaches are normalized to the same low-lying levels, the normalized NLD of ^{93}Sr obtained using either approach follows the discrete levels up to 2.2 MeV, as shown in Fig. 6a. However, using *norm*1 results in a normalized ^{93}Sr NLD that generally better reproduces

the total level density of discrete levels below 2.2 MeV as shown in Fig. 6a, except for one data point centered at E_x = 90 keV. The extracted ^{93}Sr NLD is then best normalized using the *norm*1 approach for high excitation energy and discrete levels at low excitation energy below 2.2 MeV [24]. In the energy region between the collected data and the estimated $\rho(S_n)$ for *norm*1, the CT model was used to interpolate the NLD, represented by the dashed line in Fig. 6a, and expressed by the equation [43]:

$$\rho_{CT}(E_x) = \frac{1}{T}\exp^{\frac{E_x - E_0}{T}}, \tag{12}$$

where the nuclear temperature, T, and excitation-energy shift, E_0. For the *norm*1 approach, different slopes, or nuclear temperatures T, of the NLD result from the upper and lower estimated $\rho(S_n)$ values. This systematic uncertainty is illustrated by the violet band and also corresponds to differently-sloped γSFs. For the *norm*2 approach, the HFB + c tabulated level density was used for interpolation, as shown by a dashed line, between the collected data and the microscopic level density calculation at S_n. The resulting NLD obtained using *norm*2 is steeper than the slope obtained using *norm*1, and consequently, leads to a steeper γSF that is discussed in Section IV B 1. Due to the uncertainty of the estimated value for $\rho(S_n)$ used in *norm*1, the upper and lower limits of the normalized NLD yielded an upper deviation of 15% and a lower deviation of 9%, on average, which are shown as bounds of the violet shaded region in Fig. 6a.

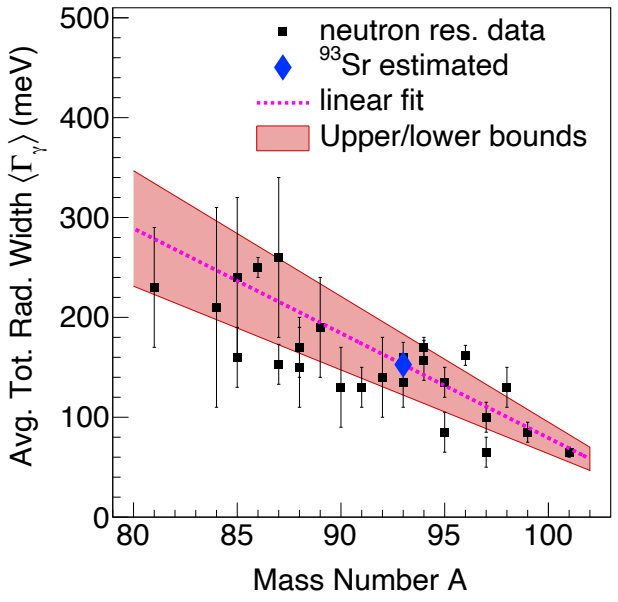

FIG. 5. Estimated average, total radiative width, $\langle\Gamma_\gamma(S_n)\rangle$, for ^{93}Sr (blue diamond) based on a linear fit of the known values for ^{81,84,85,87}Kr, ^{86,88}Rb, ^{85,87,88,89}Sr, ^{90}Y, ^{91,92,93,94,95,97}Zr, ^{94}Nb, and ^{93,95,96,97,98,99,101}Mo (black squares). The error band, indicated by the red-shaded region, shows the 1-σ χ^2 minimization of the neutron resonance data.

B. Normalizing the γSF

1. *γSF slope obtained using auxiliary nuclear data*

In order to obtain the γSF normalization, we utilized systematics of neutron resonance parameters for the Kr, Rb, Sr, Y, Zr, Nb, and Mo isotopes which is summarized here. This approach was implemented to determine the B parameter in Eq. 6. The α parameter was already obtained from the NLD normalization to discrete levels and an estimated $\rho(S_n)$ for ^{93}Sr. The final parameter B can be derived from the relationship between the total, average radiative width, $\langle\Gamma_\gamma(S_n)\rangle$, and the transmission coefficient of dipole transitions, $\mathcal{T}(E_\gamma)$, or the γSF [5, 9]. If the γSF is expressed in terms of only dipole transitions, Eq. 3 becomes

$$B\mathcal{T}(E_\gamma) = [f_{E1}(E_\gamma) + f_{M1}(E_\gamma)]E_\gamma^3, \tag{13}$$

which can be expanded further to highlight the relationship between B and $\langle\Gamma(S_n, J_t \pm 1/2, \pi_t)\rangle$ for neutron s-wave capture resonances with spins $J_t \pm 1/2$ as shown by Ref. [33] and expressed as

$$\langle\Gamma(S_n, J_t \pm 1/2, \pi_t)\rangle = \frac{1}{2\rho(S_n, J_t \pm 1/2, \pi_t)} \int_{E_\gamma=0}^{S_n} dE_\gamma B\mathcal{T}(E_\gamma)\rho(S_n - E_\gamma)\times \sum_{j=-1}^{1} g(S_n - E_\gamma, J_t \pm 1/2 + j), \tag{14}$$

where J_t and π_t are the target spin and parity, $g(E_x, J)$ is the spin distribution function, and $\rho(S_n - E_\gamma)$ is the total level density at a final energy. Equation 14 highlights the interdependence between the NLD and the γSF, thus the systematic uncertainty in normalizing the NLD using an estimated $\rho(S_n)$ is propagated to the normalized γSF when solving for $\mathcal{T}(E_\gamma)$.

The third normalization parameter B was determined using systematics for the neighboring nuclei ^{81,84,85,87}Kr, ^{86,88}Rb, ^{85,87,88,89}Sr, ^{90}Y, ^{91,92,93,94,95,97}Zr, ^{94}Nb, and ^{93,95,96,97,98,99,101}Mo to estimate the $\langle\Gamma_\gamma\rangle$ for ^{93}Sr [36]. A linear fit of experimental $\langle\Gamma_\gamma\rangle$ values for Kr to Mo nuclei as a function of mass number A, was used to yield an estimated value for ^{93}Sr of $\langle\Gamma_\gamma\rangle$ =153±31 meV. Fig. 5 shows the neutron resonance data for these isotopes as well as the linear fit and associated uncertainty band. The fit resulted in a reduced-χ^2 >1, and so, the χ^2 uncertainty of applying a scaling factor to the linear fit was used to determine the upper and lower estimates shown by the band. As a physical reason for the linear trend between $\langle\Gamma_\gamma\rangle$ of neighboring nuclei Kr to Mo and mass number is unclear, the uncertainty of 31 meV was used to best incorporate the regional systematics. In contrast, a

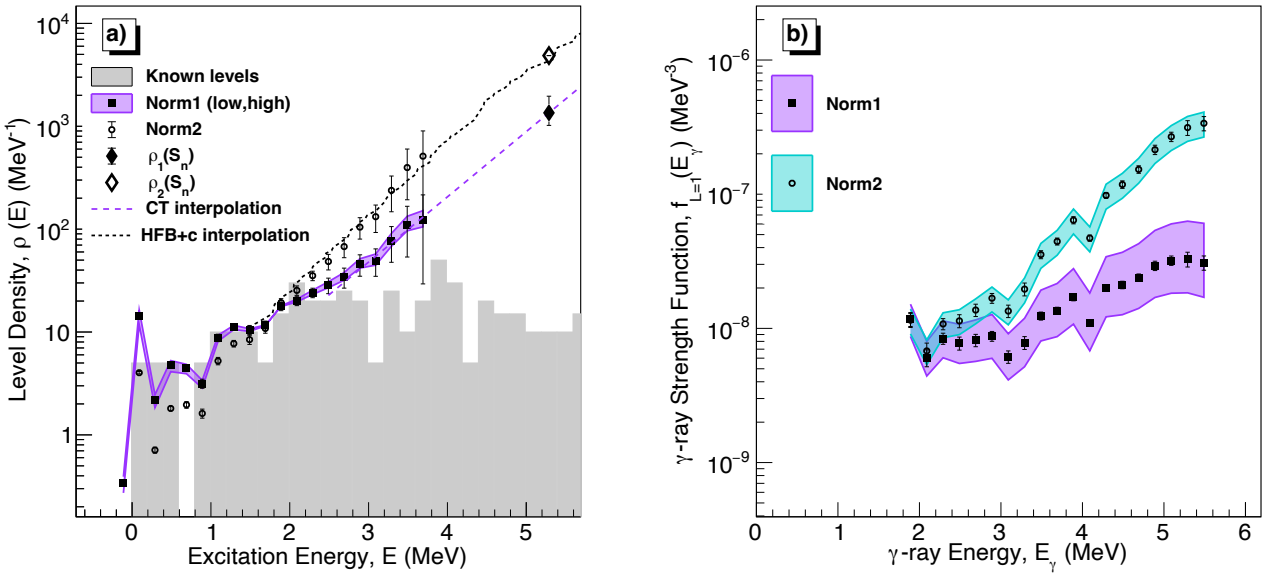

FIG. 6. (a) The extracted NLD of ^{93}Sr for two normalization approaches are illustrated by filled squares and open circles. The estimated $\rho(S_n)$ for ^{93}Sr (open and filled diamond) along with 20 discrete levels for ^{93}Sr give an upper- and lower- normalization of the NLD. Beyond the experimental data, for E_x >3.6 MeV, the NLD is interpolated to S_n using the CT model ($norm1$) or the HFB+c tabulated level density ($norm2$). (b) The extracted γSF of ^{93}Sr for the different normalization approaches. The uncertainties on the estimated $\rho(S_n)$ and $\langle\Gamma_\gamma\rangle$ for ^{93}Sr serve as upper and lower limits on the normalized γSF.

TABLE I. Parameters used in GLO fit of the ^{93}Sr γSF data: GDR parameters E_G, Γ_G, and σ_G corresponding to the centroid energy, width, and cross section as well as a constant temperature for the final states T_f. In addition to the GLO fit, the steep rise of the ^{93}Sr γSF is taken into account with two pygmy resonance described by standard Lorentzians with parameters: E_{py1}, Γ_{py1}, σ_{py1}, E_{py2}, Γ_{py2}, and σ_{py2} corresponding to the peak energy, width, and cross section. The low energy region of the γSF is characterized with an upbend function $f_{upbend}(E_\gamma) = Ce^{-\eta E_\gamma}$.

E_G (MeV)	Γ_G (MeV)	σ_G (mb)	T_f (MeV)	E_{py1} (MeV)	Γ_{py1} (MeV)	σ_{py1} (mb)	E_{py2} (MeV)	Γ_{py2} (MeV)	σ_{py2} (mb)	C (10^{-9} MeV^{-3})	η (MeV^{-1})
17.02	4.07	199	0.10	13.93	2.87	23.65	5.25	1.50	1.52	6.72	0.17

linear fit of experimental $\langle\Gamma_\gamma\rangle$ as a function neutron separation energy did not show a visible trend.

In Fig. 6b, the extracted γSFs for the different NLD normalization approaches are compared showing that the HFB+c NLD approach results in a very steep γSF slope. As it is shown in Fig. 6b the two normalizations are in disagreement, thus the available ^{88}Sr(γ, n)^{87}Sr data published by Ref. [44] was used to select $norm1$ as the appropriate approach for ^{93}Sr γSF normalization. The upper and lower limits of the normalized γSF are presented as uncertainty bands which includes the systematic uncertainty of NLD normalization approaches and the estimated $\langle\Gamma_\gamma\rangle$, where the violet-shaded region represents the uncertainty from $norm1$ and the cyan-shaded region represents the uncertainty from $norm2$. In the case of $norm1$, the resulting uncertainty band has an upper deviation of 61% and a lower deviation of 36%, on average. Furthermore, the resulting γSF from these approaches are compared to the GDR of ^{88}Sr obtained from photoabsorption cross section data in Fig. 7 [44]. To fit the γSF for ^{88}Sr, we adopted a Generalized Lorentzian (GLO) model for the E1 strength which incorporates an energy- and temperature-dependent width $\Gamma_k(E_\gamma, T_f)$ and the GDR parameters: centroid energy E_G, width Γ_G, and cross section σ_G, and is expressed by

$$f^{E1}_{GLO}(E_\gamma, T_f) = \frac{\sigma_G\Gamma_G}{3(\pi\hbar c)^2}\Big[\frac{E_\gamma\Gamma_k(E_\gamma,T_f)}{(E_\gamma^2-E_G^2)^2+E_\gamma^2\Gamma_k^2(E_\gamma,T_f)} + 0.7\frac{\Gamma_k(E_\gamma=0,T_f)}{E_G^3}\Big], \quad (15)$$

where $\Gamma_k(E_\gamma, T_f)$ is defined as

$$\Gamma_k(E_\gamma=0,T_f) = \frac{\Gamma_G}{E_G^2}(E_\gamma^2+4\pi^2T_f) \quad (16)$$

from Ref. [45]. As the GDR is predominantly characterized by E1 strength, the resulting fit yielded the following parameters: E_G=16.87(3) MeV, Γ_G = 4.25(8) MeV, and σ_G = 205(2) mb. Ref. [46] also showed that one Lorentz line fit of Rb, Sr, ^{89}Y, ^{90}Zr, and ^{93}Nb photoneutron cross sections sufficiently characterized the GDR. The GDR parameters from this initial GLO fit were then used to fit the ^{93}Sr E1 and M1 strength.

While a Generalized Lorentzian (GLO) model was used to fit the E1 strength, two standard Lorentzian functions (SLO) and an upbend function in the form of $f_{upbend}(E_\gamma) = Ce^{-\eta E_\gamma}$ was used to fit the M1 strength [45, 47]. The E1+M1 fit of the ^{88}Sr photoabsorption data along with our ^{93}Sr γSF was improved through the addition of a SLO component with parameters E_{py1}, Γ_{py1}, and σ_{py1} at ∼14 MeV, which may be related to a pygmy dipole resonance. In addition, at $E_\gamma \approx 5$ MeV a narrow pygmy described by parameters E_{py2}, Γ_{py2}, and σ_{py2} shown in Table I was assumed to connect our ^{93}Sr γSF to the ^{88}Sr photoabsorption data. A low-energy enhancement, or *upbend*, in the γSF was first observed in ^{56,57}Fe and $^{93-98}$Mo using the Oslo Method [47–49]. In addition, the phenomenon was confirmed for ^{95}Mo using an alternative model-independent technique known as the Ratio method, which obtains the energy dependence of the γSF from correlated particle-γ-γ events following direct reactions [50]. The magnitude of the upbend was constrained to $C < 6 \times 10^{-8}$ MeV during fitting of the ^{93}Sr data due to scarcity of data at lower E_γ <1.8 MeV. At low E_γ, our extracted ^{93}Sr γSF appears to be constant, and the resulting fit parameter C is an order of magnitude lower compared to the upbend structure observed in ^{89}Y and ^{91}Zr [37, 40]. Similar to our ^{93}Sr γSF, the measured ^{97}Mo(n, γ) reaction by Ref. [51] using the DANCE (Detector for Advanced Neutron Capture Experiments) array did not indicate a clear resonance structure near 2 MeV that was reported by Ref. [47]. However, in general for these previous cases from Refs. [47–49], the upbend is clearly visible below 2 MeV, which is near the γ-ray threshold used for the β-Oslo Method applied to ^{93}Sr. The sum of the GLO, pygmy, and upbend fit is illustrated with a solid red line in Fig. 7. The parameters used in the E1 and M1 strength fit are shown in Table I. Photoabsorption data from Ref. [44] were used to guide the normalization of ^{93}Sr γSF as there is an absence of photonuclear data this far from the valley of stability. The slope of the γSF obtained as a result of the phenomenological NLD model approach agrees best with the ^{88}Sr(γ, n)^{87}Sr data, while the slope of the γSF obtained from the HFB + c NLD approach is significantly steeper and compares poorly to the observed behavior of the γSF for ^{88}Sr as it approaches 11 MeV.

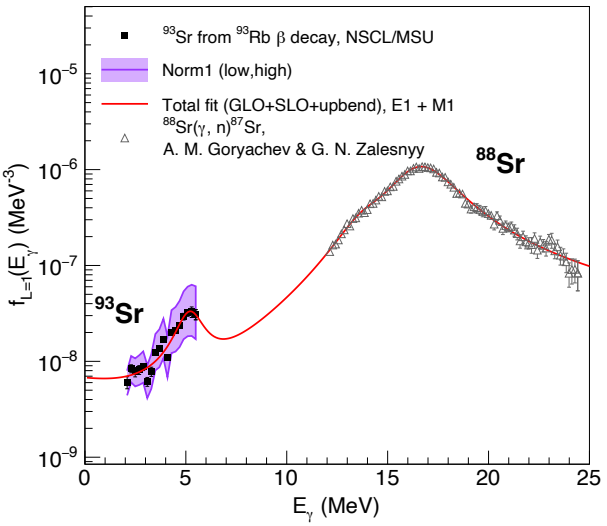

FIG. 7. The extracted γSF for ^{93}Sr (black squares) compared to the γSF for ^{88}Sr (triangles) [44]. The shaded region represents the upper- and lower-limits on the systematic uncertainty due to normalization (*norm*1) of the extracted NLD and γSF. Also shown is the total dipole-strength fit function (solid red line) which includes the GLO component for the E1 strength as well as two SLO and one upbend component for the M1 strength.

The resulting γSF of this work was extracted from the ROI of the primary γ-ray matrix in Fig. 2c, where γ decay is assumed to be statistical; however, the primary γ-ray matrix exhibits strong direct transitions to the J^π=5/2$^+$ ground state, which are clearly visible as the outermost diagonal in the $P(E_x, E_\gamma)$ matrix. In addition, strong direct transitions are also visible to the first, second, and third excited states, which have tentative spin assignments: $(9/2)^+$, (5/2, 7/2, $9/2)^+$, and $(9/2^+)$, respectively [52]. These strong γ-decay transitions could potentially undermine the β-Oslo Method assumption that the extracted NLD and γSF, *i.e.*, average nuclear properties, were obtained from a region described by a statistical process. In Fig. 8a, several regions are shown with diagonal cuts applied to the primary γ-ray matrix excluding primaries to the ground state as well as the first three excited states: 213.431(11), 432.604(24), and 986.12(5) keV. For Regions 1 and 2, the residuals between these γSF's and the γSF extracted from the entire ROI is less than 2-σ, *i.e.*, twice the value of the systematic error. For Regions 3 and 4, the residuals are less than 3-σ. Each of the selected regions in Fig. 8b are within reasonable agreement of the systematic uncertainties, and thus illustrate there is no indication of any violation of the statistical approach of this work.

2. *γSF slope obtained using the Shape Method*

In the previous section, the extracted γSF from experimental measurements of the γ-ray spectra and total absorption spectra of ^{93}Sr relied on the normalization of the NLD to obtain the slope, α, of the γSF as was previously done in the case of ^{76}Ge and ^{51}Ti [6, 11]. In con-

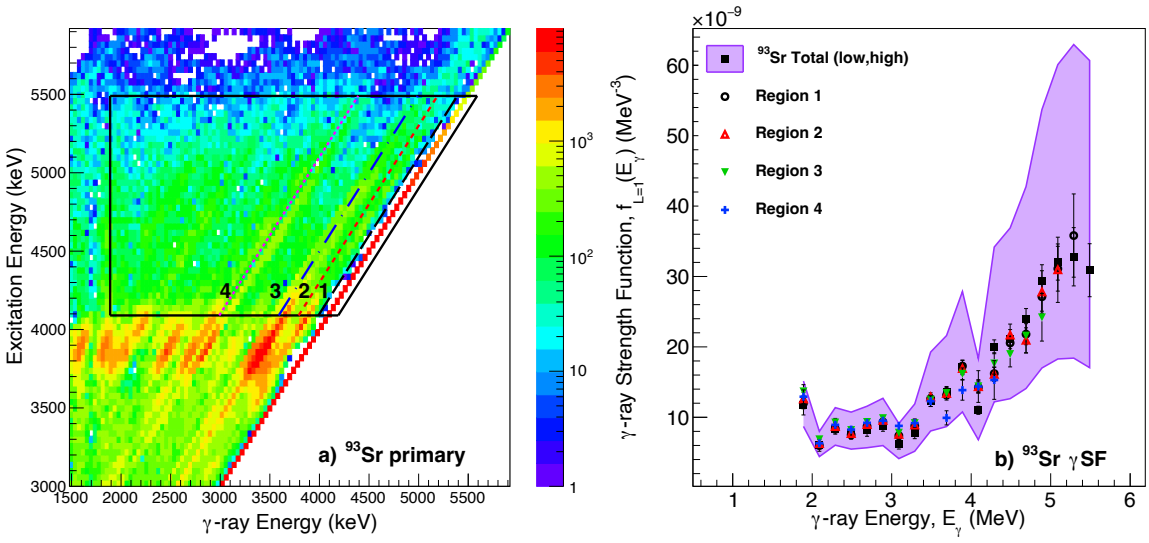

FIG. 8. (a) The extracted γSF of ^{93}Sr for the different regions of the primary γ-ray matrix. Regions 1, 2, 3, and 4 indicated with black, red, blue, and magenta dashed lines exclude the ground state and the first, second, and third excited states, respectively. (b) The γSF extracted from the total region of interest as well as systematic uncertainty (violet shaded region) due to normalization using NLD $norm1$ and estimated $\langle\Gamma_\gamma\rangle_A$ =153±31 meV are plotted adjacent to the γSFs extracted from the corresponding regions.

trast, a novel approach to obtain the shape of the γSF in the absence of an experimental D_0 value was introduced by M. Wiedeking *et al.*, referred to as the Shape Method [53]. The Shape Method was also applied to β-decay data by D. Mücher *et al.* [54]. An additional difference between the methods is that the Shape Method can be directly applied to the raw matrix of excitation energy versus γ-ray energy instead of the primary γ-ray matrix, which includes systematic uncertainties from the first two steps of the β-Oslo Method. Ref. [9] discusses the uncertainties and possible systematic errors for each step of the standard Oslo Method. A possible systematic error highlighted by Ref. [9] is the presence of vertical ridges and/or valleys at low energies in the matrix due to under and/or over subtraction of higher order γ rays when applying the primary generation method of the Oslo Method. Due to these systematic errors in the primary γ-ray matrix, the β-Oslo Method cannot be used to extract the NLD and γSF for γ-ray energies below 2.0 MeV for ^{93}Sr. Furthermore, the Shape Method is expected to successfully obtain the ^{93}Sr γSF since no non-statistical effects in transitions to the lowest states were observes as discussed in the previous section.

The Shape Method utilizes a ratio approach between the intensities for two different primary γ-ray energies from the same initial excitation energy to discrete low-lying levels visualized as a diagonal in the $P(E_x, E_\gamma)$ matrix. In addition, the method assumes symmetric parity distribution and a spin distribution $g(E, J)$, Eq. 11. In applying the Shape Method to this work, we examined the ratio of the second and third excited state, both of which have tentative spin assignments. Due to the tentative spin assignment, a γSF was obtained using the Shape Method for each combination of spin assignment for the second and third excited state as shown in Fig. 9. These combinations include spins $J = 5/2$ to $9/2$ for the second excited state E_2, while the spin of the third excited state is fixed at $J = 9/2$. The Shape Method-obtained γSFs, were scaled in magnitude to the β-Oslo Method-obtained γSF, which was normalized using $norm1$ and $\langle\Gamma_\gamma\rangle$ =153±31 meV. The resulting γSF for the selected spin assignments are in reasonable agreement with one another and are well within the systematic error shown by the violet band of the β-Oslo Method-extracted γSF. The β-Oslo Method applied to ^{93}Sr made use of a 1.89 MeV γ-ray threshold; however, the Shape Method utilized here contributes significantly to extending the γSF below $E_\gamma < 2$ MeV.

V. ^{92}SR$(n,\gamma)^{93}$SR CROSS SECTION CALCULATION

This work presents the first experimentally-constrained NLD and γSF for ^{93}Sr. These nuclear properties obtained using the β-Oslo Method are key components in calculating the neutron-capture cross section. These statistical properties, along with an optical model potential (OMP) are input parameters in the Hauser-Feshbach formalism which is used by TALYS1.95 (here after referred to as TALYS) to calculate neutron-capture cross sections [41]. Of these key components in

calculating the (n,γ) cross section, the NLD and γSF most significantly influence the systematic uncertainty of the calculation, as was previously discussed by S. N. Liddick *et al.* [7].

A. Theoretical reaction calculation of the ^{92}Sr$(n,\gamma)^{93}$Sr cross section

The theoretical ^{92}Sr(n,γ)^{93}Sr cross section was calculated using default input NLD, γSF, and OMP models in TALYS. Default input parameters include the combined constant temperature (CT) plus Fermi gas model for the NLD, the Kopecky-Uhl generalized Lorentzian for the $E1$ strength (Eq. 15) [45], an $M1$ strength as a function of the $E1$ strength: $f_{E1}/(0.0588A^{0.878})$ [41], and a Koning and Delaroche neutron OMP with local parameters [55]. A range of NLD and γSF models that include both phenomenological and microscopic approaches are plotted in Fig. 10a and 10b, respectively. The resulting calculated cross section using default model settings is shown as a black curve in Fig. 11. To obtain a maximum and minimum value for the ^{92}Sr$(n,\gamma)^{93}$Sr cross section, the combination of NLD, γSF, and OMP models were varied. The resulting cross sections bounds are as such

1. *maximum*: combined CT plus Fermi gas model for the NLD yielding D_0= 7.27 keV, Brink-Axel Lorentzian [29, 56] for $f_{E1}(E_\gamma)$ with a renormalization factor of $\langle\Gamma_\gamma\rangle$= 150 meV obtained from an interpolation table for $40 < A < 150$ [41], $f_{E1}/(0.0588A^{0.878})$ for the $f_{M1}(E_\gamma)$, and Koning and Delaroche OMP with local parameters [55],

2. *minimum*: a microscopic approach based on Skyrme force for the NLD yielding D_0= 21.74 keV from Ref. [39], a microscopic approach based on Gogny D1M force and combined Hartree-Fock-Bogoliubov (HFB) plus quasiparticle-random-phase approximation (QRPA) yielding $\langle\Gamma_\gamma\rangle$= 25.72 meV [41, 57], $f_{E1}/(0.0588A^{0.878})$ for the $f_{M1}(E_\gamma)$, and Koning and Delaroche OMP with global parameters.

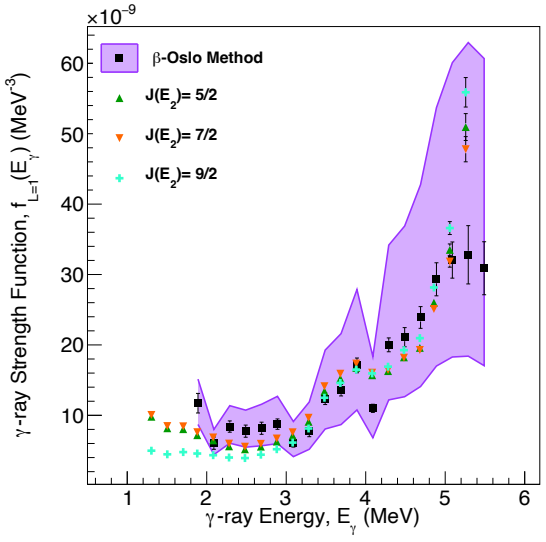

FIG. 9. The extracted γSF for ^{93}Sr (black squares) compared to the γSF extracted using the Shape Method. Using the Shape Method, the spin assignment of the second excited state $E_2 = 432$ keV were varied while the spin of the third excited state $E_3 = 986$ keV is kept fix at $J(E_3) = 9/2$. All Shape Method extracted γSF's are within the systematic error of the β-Oslo Method normalization approaches shown by the violet shaded region. The error bars of the Shape Method-extracted γSF's are obscured by the markers.

The range of TALYS-available NLD models for ^{92}Sr(n,γ)^{93}Sr was compared to this work shown in Fig. 10a. In the high excitation energy region, 2.3 MeV to 3.7 MeV, the difference between the upper and lower model NLD was on average a factor of 15 larger than the systematic uncertainty quantified in this work. In the case of the NLD, the theoretically predicted NLDs for ^{93}Sr are steeper than the NLD extracted in this work, which consequently leads to a steeper γSF that presents a mismatch with the characteristics of the ^{88}Sr GDR. Additionally, the comparison highlights the relatively small uncertainty due to the NLD normalization approach.

Similarly, Fig. 10b illustrates a comparison between the γSF extracted in this work and the available γSF models in TALYS, which reveals a significant amount of overlap between theoretically predicted values and the experimental data. The TALYS model variations of the γSF, represented as a band spanning from the lower to upper theoretical prediction of the γSF in Fig. 10b, are on average a factor of 26 larger than the experimental statistical uncertainty and a factor of four larger than the experimental band representing the uncertainty due to normalization. The experimentally-determined γSF is impacted most by the uncertainty due to normalization that propagated the systematic uncertainty from the NLD, *i.e.*, the α factor describing the slope of both the NLD and γSF, as well as the estimated value of the $\langle\Gamma_\gamma\rangle$. Though the normalization approach employed in this work lacked neutron resonance data specifically for ^{93}Sr, our estimated value for $\rho(S_n)$ and $\langle\Gamma_\gamma\rangle$ significantly constrained the NLD and γSF compared to previous theoretical predictions.

The theoretical NLD, γSF, and OMP models used to calculate the (n,γ) cross section vary significantly, so much so that the ratio between the upper and lower bounds is ≈12 on average for 10 keV $< E_n <$ 5 MeV. Fig. 11 illustrates the maximum and minimum calculated cross sections using the avalaible models represented by a grey-shaded band.

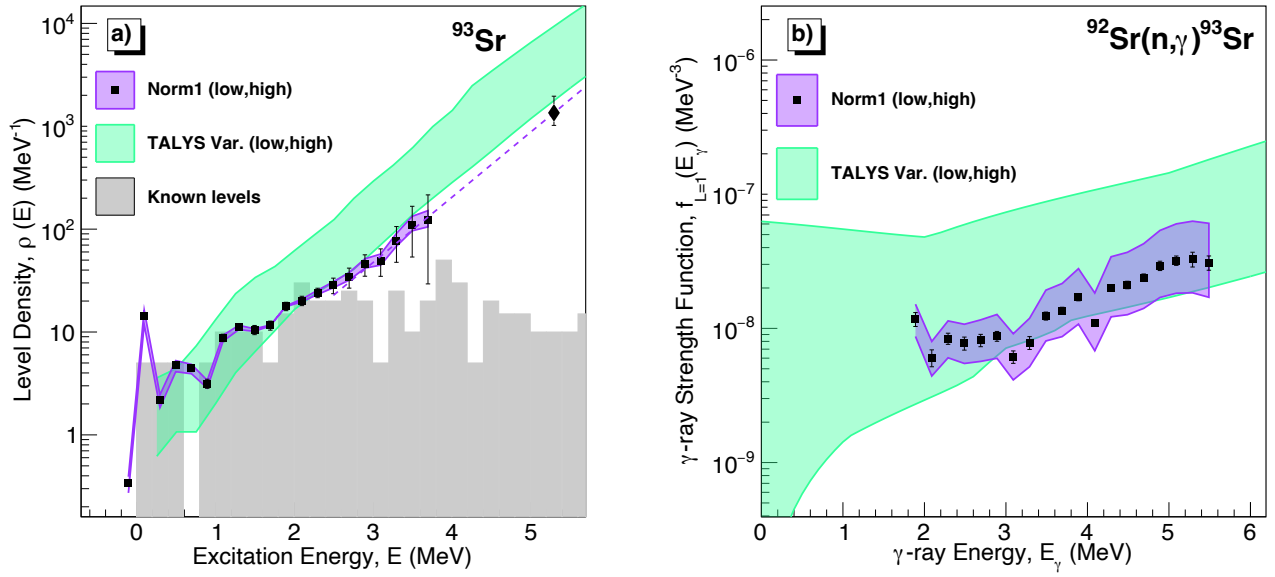

FIG. 10. (a) The ^{93}Sr NLD obtained by this work is compared to the six TALYS level density models shown as a teal band. (b) The ^{93}Sr γSF obtained by this work is compared to the eight TALYS strength models, where the upper and lower limits of the teal bands represent the maximum and minimum predicted values from these models.

B. ^{92}Sr$(n,\gamma)^{93}$Sr cross section calculation from this work

The ^{92}Sr$(n,\gamma)^{93}$Sr cross section was calculated using the experimentally-determined NLD and γSF and all corresponding uncertainties. The extracted NLD with a CT interpolation to S_n described in Sec. IV A for energies above E_x=2.2 MeV and the total level density of discrete states below 2.2 MeV were used to calculate the (n,γ) cross section. The γSF presented in this work for 1.89 MeV $< E_\gamma <$ 5.49 MeV was utilized in the TALYS calculation along with the total dipole-strength fit function discussed in Section IV B to extrapolate the strength above 5.49 MeV to the GDR and below 1.89 MeV. In calculating the neutron-capture cross section, both the Koning and Delaroche neutron OMP (nOMP) with local parameters and the semimicroscopic optical potential of the Jeukenne–Lejeune–Mahaux (JLM) OMP were examined and included in the violet systematic uncertainty band in Fig. 11 [41, 58]. On average for 10 keV $< E_n <$ 5 MeV, the selection of nOMP or JLM resulted in less than one percent difference in the neutron-capture cross section calculated. The resulting ^{92}Sr$(n,\gamma)^{93}$Sr cross section calculated using the nOMP approach is shown as black crosses in Fig. 11 with an uncertainty band in violet representative of the normalization approaches discussed in Secs. IV A and IV B. This experimentally-determined ^{92}Sr$(n,\gamma)^{93}$Sr cross section is lower than several TALYS calculated cross sections using theoretical models as nuclear structure inputs represented by the grey-shaded band in Fig. 11.

The normalization approaches used in this work decreased the uncertainty on the ^{92}Sr(n,γ)^{93}Sr cross section compared to predicted values. The ratio between the upper- and lower-bound cross section limits was, on average, approximately three for 10 keV $< E_n <$ 5 MeV. The calculated neutron-capture cross section using experimentally-determined NLD and γSF falls within the lower limits of the uncertainty band provided by theoretical predictions; however, the resulting cross section does not agree with the default TALYS prediction. A lower neutron-capture reaction has potentially meaningful impact on astrophysical abundance calculations and fission product burnup calculations by lowering the predicted production of heaver Sr isotopes through neutron capture [1, 16, 49].

The uncertainty of the γSF obtained using the Shape Method, which investigated the combination of spin assignments for the second and third excited states, resulted in cross section uncertainties that were smaller than those of the normalization approaches discussed in Secs. IV A and IV B, and as such, the predominant uncertainty inherent to the calculated cross section is due to the contribution of the uncertainty of the estimated $\rho(S_n)$ and $\langle\Gamma_\gamma\rangle$ values.

VI. SUMMARY AND CONCLUSION

In this work, the β-Oslo Method was used to analyze γ-ray spectra following the β decay of a radioactive beam

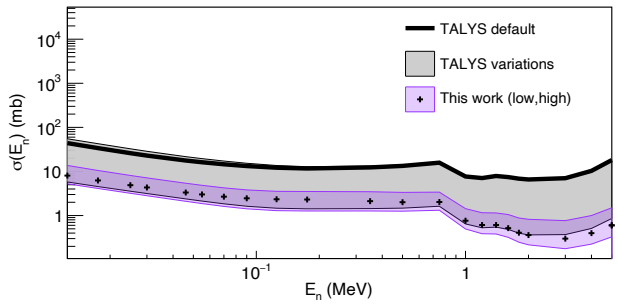

FIG. 11. Experimentally-determined ^{92}Sr(n,γ)^{93}Sr cross section (crosses) along with systematic uncertainty shown as a violet-shaded band compared to theoretical predictions and the default TALYS calculated cross section. These theoretical calculations of the cross sections using variations in phenomenological models and microscopic models are represented by a grey-shaded band, while the default calculation is illustrated by the black curve.

of ^{93}Rb obtained using the SuNTAN detector system at the NSCL in order to experimentally determine the NLD and γSF for ^{93}Sr. The resulting ^{92}Sr(n,γ)^{93}Sr cross section uncertainty, or the difference between the upper and lower limits, associated with the normalization approaches used to determine these key statistical nuclear properties was characterized and found to be factor of six smaller than the theoretically-predicted cross section uncertainty. Our work, therefore, illustrates that the process of constraining statistical nuclear properties can be significantly improved using neutron resonance spacing data, even in challenging cases where experimental nuclear structure details are incomplete, such as when normalizing the NLD and γSF of a neutron-rich isotopes. This work found the NLD of ^{93}Sr displays a behavior similar to the CT formula and best described using an energy-dependent spin-cutoff parameter to estimate the total level density at the neutron separation energy. The γSF of ^{93}Sr can be described predominantly by a Generalized Lorentzian along with a structure that may be related to a pygmy dipole resonance near the neutron separation energy.

Additionally, the γSF for ^{93}Sr produced in this work exhibited a flattening of the strength function, rather than an observable *upbend*, at low E_γ, as has been observed in this mass region in the cases of ^{89}Y and ^{76}Ge [6, 37]. In this case, a constant γSF at low γ-ray energies was observed as well as a lower overall value for the experimentally constrained neutron-capture cross section compared to the TALYS default calculation, which has potential ramifications for astrophysical calculations of heavy element production and burnup of fission-products in high neutron-flux environments through a reduced neutron-capture reaction rate [1, 16].

Radioactive isotope beams with high intensities and high purity, provided by such facilities as the Facility for Rare Isotope Beams (FRIB) at Michigan State University (MSU) and the Californium Rare Isotope Breeder Upgrade (CARIBU) facility at Argonne National Laboratory, along with the SuNTAN detector system, are key tools to achieving successful β-Oslo experiments investigating nuclei away from the valley of stability. While the case of ^{93}Sr was challenging due to the gaps in nuclear structure data for a nucleus five nucleons away from stability, the ability to constrain statistical nuclear properties will only increase in difficulty as the neutron-drip line is approached. In addition to the challenges of providing reliable normalization approaches in these cases, very-neutron-rich nuclei have low neutron separation energies and high β-delayed neutron branches, which results in a smaller statistical region to which the β-Oslo Method can be applied. For such exotic nuclei, challenges also remain in measuring the γ-ray spectra due to the β-decay chain, which results in a γ-ray contribution that is difficult to distinguish from the decays of interest. Such experiments on exotic nuclei are imperative to pursue as they improve our understanding of neutron-induced reactions which have a wide range of impact on understanding astrophysical processes and fission product burnup.

VII. ACKNOWLEDGEMENT

The authors would like to thank the operations team at the National Superconducting Cyclotron Laboratory for providing the radioactive isotope beam, data-user space, and beam physics technical support. The authors would also like to thank colleagues at the University of Oslo for their mentorship and guidance. This work was performed under the auspices the U.S. Department of Energy by Lawrence Livermore National Laboratory under Contract DE-AC52-07NA27344 and Lawrence Berkeley National Laboratory under Contract No. DE-AC02-05CH11231. This research was supported by Michigan State University and the Facility for Rare Isotope Beams and was funded in part by the NSF under Contracts No. PHY- 1102511 (NSCL), No. 1350234 (CAREER), No. 1430152 (JINA-CEE), the National Nuclear Security Administration under Award No. DE-NA0000979, DE-NA0003180, DE-NA0003906, and DE-NA0003996, and U.S. Department of Energy, Office of Science, Office of Nuclear Physics, under Grants No. DE-SC0020451. A.C.L. gratefully acknowledges funding from the ERC-STG-2014 under grant agreement no. 637686, and support from the ChETEC COST Action (CA16117), supported by COST (European Cooperation in Science and Technology). M.W. acknowledges support from the National Research Foundation of South Africa under Grant No. 118846.

[1] J. Carlson, M. P. Carpenter, R. Casten, C. Elster, P. Fallon, A. Gade, *et al.*, Progress in Particle and Nuclear Physics **94**, 68 (2017).
[2] J. E. Escher, J. T. Harke, F. S. Dietrich, N. D. Scielzo, I. J. Thompson, and W. Younes, Rev. Mod. Phys. **84**, 353 (2012).
[3] A. Ratkiewicz, J. A. Cizewski, J. E. Escher, G. Potel, J. T. Harke, R. J. Casperson, *et al.*, Phys. Rev. Lett. **122**, 052502 (2019).
[4] M. Guttormsen, T. Ramsøy, and J. Rekstad, Nucl. Instrum. Methods Phys. Res. Sect. A **255**, 518 (1987).
[5] A. Schiller, L. Bergholt, M. Guttormsen, E. Melby, J. Rekstad, and S. Siem, Nucl. Instrum. Methods Phys. Res. Sect. A **447**, 498 (2000).
[6] A. Spyrou, S. N. Liddick, A. C. Larsen, M. Guttormsen, K. Cooper, A. C. Dombos, *et al.*, Phys. Rev. Lett. **113**, 232502 (2014).
[7] S. N. Liddick, A. Spyrou, B. P. Crider, F. Naqvi, A. C. Larsen, M. Guttormsen, *et al.*, Phys. Rev. Lett. **116**, 242502 (2016).
[8] N. Bohr, Nature **137(3461)**, 344 (1936).
[9] A. C. Larsen, M. Guttormsen, M. Krtička, E. Běták, A. Bürger, A. Görgen, H. T. Nyhus, J. Rekstad, A. Schiller, S. Siem, H. K. Toft, G. M. Tveten, A. V. Voinov, and K. Wikan, Phys. Rev. C **83**, 034315 (2011).
[10] T. A. Laplace, F. Zeiser, M. Guttormsen, A. C. Larsen, D. L. Bleuel, L. A. Bernstein, *et al.*, Phys. Rev. C **93**, 014323 (2016).
[11] S. N. Liddick, A. C. Larsen, M. Guttormsen, A. Spyrou, B. P. Crider, F. Naqvi, *et al.*, Phys. Rev. C **100**, 024624 (2019).
[12] W. Hauser and H. Feshbach, Phys. Rev. **87**, 366 (1952).
[13] S. Goriely, The European Physical Journal A **51**, 1 (2015).
[14] T. Kajino, W. Aoki, A. Balantekin, R. Diehl, M. Famiano, and G. Mathews, Progress in Particle and Nuclear Physics **107**, 109 (2019).
[15] E. M. Burbidge, G. R. Burbidge, W. A. Fowler, and F. Hoyle, Rev. Mod. Phys. **29**, 547 (1957).
[16] P. Denissenkov, G. Perdikakis, F. Herwig, H. Schatz, C. Ritter, M. Pignatari, S. Jones, S. Nikas, and A. Spyrou, J. Phys. G Nucl. Partic. **45**, 055203 (2018).
[17] F. Marti, P. Miller, D. Poe, M. Steiner, J. Stetson, and X. Y. Wu, AIP Conference Proceedings **600**, 64 (2001).
[18] D. J. Morrissey, B. M. Sherrill, M. Steiner, A. Stolz, and I. Wiedenhoever, Nucl. Instrum. Methods Phys. Res. Sect B **204**, 90 (2003).
[19] A. Simon, S. J. Quinn, A. Spyrou, A. Battaglia, I. Beskin, A. Best, *et al.*, Nucl. Instrum. Methods Phys. Res. Sect A **703**, 16 (2013).
[20] K. Cooper, C. S. Sumithrarachchi, D. J. Morrissey, A. Levand, J. A. Rodriguez, G. Savard, and B. . Zabbransky, Nucl. Instrum. Methods Phys. Res. Sect A **7663**, 543 (2014).
[21] C. M. Harris, M. K. Smith, F. Naqvi, *et al.*, In preparation (2022).
[22] E. Rutherford, *Radio-activity* (1905) p. 331.
[23] H. Bateman, **15**, 423 (1910).
[24] C. M. Baglin, Nuclear Data Sheets **112**, 1163 (2011).
[25] P. Hoff, Nuclear Physics A **359**, 9 (1981).
[26] M. Guttormsen, T. S. Tveter, L. Bergholt, F. Ingebretsen, and J. Rekstad, Nucl. Instrum. Methods Phys. Res. Sect. A **374**, 371 (1996).
[27] S. Agostinelli, J. Allison, K. Amako, J. Apostolakis, H. Araujo, P. Arce, *et al.*, Nuclear Instruments and Methods in Physics Research Section A: Accelerators, Spectrometers, Detectors and Associated Equipment **506**, 250 (2003).
[28] D. M. Brink, Ph.D. thesis, Oxford University (1955).
[29] P. Axel, Phys. Rev. **126**, 671 (1962).
[30] M. Guttormsen, A. C. Larsen, A. Görgen, T. Renstrøm, S. Siem, T. G. Tornyi, and G. M. Tveten, Phys. Rev. Lett. **116**, 012502 (2016).
[31] M. Guttormsen, A. C. Larsen, A. Bürger, A. Görgen, S. Harissopulos, M. Kmiecik, T. Konstantinopoulos, M. Krtička, A. Lagoyannis, T. Lönnroth, K. Mazurek, M. Norrby, H. T. Nyhus, G. Perdikakis, A. Schiller, S. Siem, A. Spyrou, N. U. H. Syed, H. K. Toft, G. M. Tveten, and A. Voinov, Phys. Rev. C **83**, 014312 (2011).
[32] L. C. Campo, M. Guttormsen, F. L. Bello Garrote, T. K. Eriksen, F. Giacoppo, A. Görgen, K. Hadynska-Klek, M. Klintefjord, A. C. Larsen, T. Renstrøm, E. Sahin, S. Siem, A. Springer, T. G. Tornyi, and G. M. Tveten, Phys. Rev. C **98**, 054303 (2018).
[33] A. Voinov, M. Guttormsen, E. Melby, J. Rekstad, A. Schiller, and S. Siem, Phys. Rev. C **63**, 044313 (2001).
[34] T. von Egidy and D. Bucurescu, Phys. Rev. C **80**, 054310 (2009).
[35] T. von Egidy and D. Bucurescu, Phys. Rev. C **72**, 044311 (2005).
[36] R. Capote, M. Herman, P. Obložinský, P. G. Young, S. Goriely, T. Belgya, *et al.*, Nuclear Data Sheets **110(12)**, 3107 (2009).
[37] A. C. Larsen, M. Guttormsen, R. Schwengner, D. L. Bleuel, S. Goriely, S. Harissopulos, F. L. Bello Garrote, Y. Byun, T. K. Eriksen, F. Giacoppo, A. Görgen, T. W. Hagen, M. Klintefjord, T. Renstrøm, S. J. Rose, E. Sahin, S. Siem, T. G. Tornyi, G. M. Tveten, A. V. Voinov, and M. Wiedeking, Phys. Rev. C **93**, 045810 (2016).
[38] T. von Egidy and D. Bucurescu, Phys. Rev. C **73**, 049901(E) (2006).
[39] S. Goriely, S. Hilaire, and A. J. Koning, Phys. Rev. C **78**, 064307 (2008).
[40] M. Guttormsen, S. Goriely, A. C. Larsen, A. Görgen, T. W. Hagen, T. Renstrøm, S. Siem, N. U. H. Syed, G. Tagliente, H. K. Toft, H. Utsunomiya, A. V. Voinov, and K. Wikan, Phys. Rev. C **96**, 024313 (2017).
[41] A. J. Koning, S. Hilaire, and M. C. Duijvestijn, International Conference on Nuclear Data for Science and Technology, EDP Sciences , 211 (2007).
[42] A. Gilbert and A. G. W. Cameron, Can. J. Phys. **43**, 1446 (1965).
[43] T. Ericson, Nucl. Phys. **11**, 481 (1959).
[44] A. M. Goryachev and G. N. Zalesnyy, Vopr. Teor. Yad. Fiz. **8**, 121 (1982).
[45] J. Kopecky and M. Uhl, Phys. Rev. C **41**, 1941 (1990).
[46] A. Lepretre, H. Beil, R. Bergere, P. Carlos, A. Veyssiere, and M. Sugawara, Nuclear Physics A **175**, 609 (1971).
[47] M. Guttormsen, R. Chankova, U. Agvaanluvsan, E. Algin, L. A. Bernstein, F. Ingebretsen, *et al.*, Phys. Rev. C **71**, 044307 (2005).

[48] A. Voinov, E. Algin, U. Agvaanluvsan, T. Belgya, R. Chankova, M. Guttormsen, G. E. Mitchell, J. Rekstad, A. Schiller, and S. Siem, Phys. Rev. Lett. **93**, 142504 (2004).
[49] A. C. Larsen and S. Goriely, Phys. Rev. C **82**, 014318 (2010).
[50] M. Wiedeking, L. A. Bernstein, M. Krtička, D. L. Bleuel, J. M. Allmond, M. S. Basunia, *et al.*, Phys. Rev. Lett. **108**, 162503 (2012).
[51] C. L. Walker, M. Krtička, B. Baramsai, F. Bečvář, T. A. Bredeweg, A. Chyzh, R. C. Haight, M. Jandel, J. Kroll, G. E. Mitchell, J. M. O'Donnell, R. S. Rundberg, J. L. Ullmann, S. Valenta, and J. B. Wilhelmy, Phys. Rev. C **92**, 014324 (2015).
[52] Data extracted using the ENSDF online data serviced maintained by the NNDC; 2017-09-29.
[53] M. Wiedeking, M. Guttormsen, A. C. Larsen, F. Zeiser, A. Görgen, S. N. Liddick, D. Mücher, S. Siem, and A. Spyrou, Phys. Rev. C **104**, 014311 (2021).
[54] D. Mücher, A. Spyrou, M. Wiedeking, M. Guttormsen, A. C. Larsen, F. Zeiser, C. Harris, A. L. Richard, M. K. Smith, A. Görgen, S. N. Liddick, S. Siem, H. C. Berg, J. A. Clark, P. A. DeYoung, A. C. Dombos, B. Greaves, L. Hicks, R. Kelmar, S. Lyons, J. Owens-Fryar, A. Palmisano, D. Santiago-Gonzalez, G. Savard, and W. W. von Seeger, Phys. Rev. C **107**, L011602 (2023).
[55] A. J. Koning and J. P. Delaroche, Nucl. Phys. A **713**, 231 (2003).
[56] D. M. Brink, Nucl. Phys. **4**, 215 (1957).
[57] S. Hilaire, M. Girod, S. Goriely, and A. J. Koning, Phys. Rev. C **86**, 064317 (2012).
[58] J. P. Jeukenne, A. Lejeune, and C. Mahaux, Phys. Rev. C **15**, 10 (1977).